J. Fluid Mech. (1982), *vol.* 120, *pp.* 475–504
Printed in Great Britain

The mixing of passive helium and temperature fluctuations in grid turbulence

By A. SIRIVAT AND Z. WARHAFT

Sibley School of Mechanical and Aerospace Engineering, Cornell University, Ithaca, New York 14853, U.S.A.

(Received 28 July 1981 and in revised form 8 December 1981)

By producing thermal fluctuations with a *mandoline* and helium fluctuations with chimneys attached to the grid bars, the mixing of temperature and helium fluctuations as well as the decay of temperature and helium variance and their flux is investigated in decaying grid-generated turbulence. The helium, temperature and velocity fluctuations were measured with a modified 'Way–Libby' interference probe (Way & Libby 1970, 1971). It is shown that, as for temperature variance, the helium-variance decay rate is a function the ratio of the helium length scale to the velocity length scale. It is also shown that the decay of the cross-correlation between temperature and helium fluctuations is slow if both scalars are introduced close to the grid, but rapid if each scalar is introduced at a different distance from the grid, and hence at different scales. The results corroborate those of the inference method of Warhaft (1981), which is extended here to examine other cases. A particularly unexpected finding is that under certain circumstances the two-scalar cross-correlation may actually increase with distance from the grid, although the scalar covariance decreases. The return to isotropy of helium flux and temperature flux is also investigated and is shown to be slow if the scalar flux is produced near the grid bars, but faster if the flux is produced further downstream. For all the measurements helium and temperature were passive additives.

1. Introduction

We address here, from an experimental viewpoint, the mixing of temperature and helium fluctuations, θ and c respectively, in grid-generated turbulence. Our objective is to examine the rate of decay of such quantities as the temperature and helium variance $\overline{\theta^2}$ and $\overline{c^2}$, the longitudinal heat and concentration flux $\overline{u\theta}$ and $\overline{uc}$, and the scalar covariance $\overline{\theta c}$, as well as their associated cross-correlation coefficients $\rho_{u\theta}$, ρ_{uc} and $\rho_{\theta c}$. We will pay particular attention to the way the scalars are introduced into the flow. Here, for simplicity, the fluxes have been written in kinematic units, since the density and specific heat are constant for the flows (in which temperature and helium are passive additives) to be examined.

The reason for our study is two-fold. First, there is a practical need for information on scalar mixing in turbulent flows; data on scalar-mixing rates is needed for the prediction of chemical reaction and combustion rates as well as for an understanding of heat and mass transfer in the atmosphere and the oceans. Clearly, these engineering and natural flows are very complex, involving anisotropy, buoyancy and other production mechanisms, while the mixing of passive scalars in grid turbulence occurs in an approximately isotropic flow and without production. However, we believe it is

necessary to gain an understanding of mixing in simple flows before we attempt the more complex ones.

Secondly, there is at present a very rapid development of various modelling and computational techniques in turbulent flows. For example, for the problem of modelling scalar-variance decay in grid turbulence at least six different techniques have been used in recent years. These include second-order modelling (Newman, Launder & Lumley 1981), modelling based on Richardson dispersion arguments (Nelkin & Kerr 1981), a Lagrangian dispersion model (Durbin 1981), direct spectral simulation (Kerr 1981), large-eddy simulation (Antonopoulos-Domis 1981), and the direct-interaction approximation (Newman & Herring 1979). A particularly encouraging aspect of the three last listed techniques is that they are now able to deal computationally with the moderately large Reynolds and Péclet numbers produced in laboratory flows.† However, the way the scalar variance or covariance is introduced into the flow plays a vital role in its subsequent evolution, and this information can be properly supplied only by the experimentalist. For example, heating a grid produces a heat flux which decays very slowly with time, while introducing the thermal fluctuations far downstream from the grid, in the region where the velocity field has become approximately isotropic, produces a rapidly decaying heat flux (Warhaft & Lumley 1978*b*). The modeller and theoretician must be supplied with the proper initial conditions, or otherwise his modelling attempts may be in vain.

We have examined in our previous studies a number of aspects of scalar mixing. Warhaft & Lumley (1978*a*, *b*) have examined the decay of $\overline{\theta^2}$ and $\overline{u\theta}$ and Warhaft (1981) has used an inference method to determine scalar covariance decay. In all these studies only a single scalar, temperature, has been used. Here, we introduce a second scalar, helium, and as for temperature we pay particular attention to the way it is fed into the flow. One of our aims is to determine whether helium variance and its flux behaves in a similar manner to temperature, inspite of the necessarily different way of introducing the helium fluctuations. Another aim is to determine whether the two-scalar covariance $\overline{\theta c}$, its decay rate being a vital parameter in determining reaction rates, behaves in the same manner as the two-scalar covariance decay deduced using a single scalar which has been recently described by Warhaft (1981).

Apart from the inference method of Warhaft (1981) there appear to have been no previous experiments concerning the mixing of two scalars in grid turbulence; indeed there does not seem to be any quantitative experimental data on two-scalar mixing in any type of turbulent flow. We note that Gibson & Schwarz (1963) examined the decay rates of the variance of two different scalars, salinity and temperature in water, but they did not study the evolution and decay of the scalar covariance and flux, nor did they vary the input conditions of the scalars.

2. The apparatus

2.1. *The wind tunnel and grid*

The vertically oriented open-circuit wind tunnel was the same as that used in our previous studies (Warhaft 1981). However, in order to conserve helium gas, the test-

† Second-order modelling (in the form used by Newman *et al.* 1981) and the Richardson dispersion model are limited to very large Reynolds numbers only, and are Reynolds-number independent in this range. Durbin's scheme covers a wide Péclét-number range, and he specifically investigates the dependence of scalar variance decay on Pe.

ν (m^2/s)	$1{\cdot}65 \times 10^{-5}$
U (m/s)	4·7
M (m)	0·0125
$R_M \equiv UM/\nu$	3560
$\overline{u^2}/U^2 = A(x/M)^{-n}$ $\begin{cases} n \\ A \end{cases}$	1·33 0·0845
$\overline{u^2}$ (m/s)^2	$9{\cdot}27 \times 10^{-3}$
$l = (\overline{u^2})^{\frac{3}{2}}/\epsilon$ (m)	$6{\cdot}93 \times 10^{-3}$
$\epsilon = -\frac{3}{2}\frac{d\overline{u^2}}{dt}$ (m^2/s^3)	0·129
$\overline{v_k^2} = \nu^{\frac{1}{2}}\epsilon^{\frac{1}{2}}$ (m^2/s^2)	$1{\cdot}46 \times 10^{-3}$
$k_k = (\epsilon/\nu^3)^{\frac{1}{4}}$ (m^{-1})	$2{\cdot}31 \times 10^3$
Peak of 3-dimensional spectrum (m^{-1})	167

TABLE 1. Velocity flow parameters. The fluctuation parameters are calculated for $x/M = 54$.

section area was reduced from the original 40×40 cm^2 to 20×20 cm^2 by means of a 4 : 1 secondary contraction. The turbulence-generating grid (placed, of course, after the secondary contraction) was a biplane arrangement of 0·23 cm hollow square-sectioned brass rods with a mesh length M of 1·25 cm. Thus the solidity of the grid was 0·34, the same as that for our previous measurements in the larger wind tunnel. Most measurements were carried out at a mean test-section speed U of 4·7 m/s, giving a grid Reynolds number ($R_M = UM/\nu$) of 3560. Although this is a relatively low R_M, previous studies (Comte-Bellot & Corrsin 1966) have shown that the velocity variance decay rate at these Reynolds numbers is similar to that at higher R_M. Our results corroborate this; both the velocity and thermal variance decay and their spectra are similar to our previous measurements done at $R_M = 10\,000$ (see §3). The transverse homogeneity of the velocity field was comparable to that of our previous studies; there were deviations in the mean velocity of a few per cent and deviations of the fluctuating velocity of about 4–5 % across the core of the flow, which was approximately 11 mesh lengths wide (in both the y/M and z/M directions) at $x/M = 40$ and 8 mesh lengths wide at $x/M = 100$. The ratio u/v of the longitudinal to transverse fluctuating velocity was 1·03 at $x/M = 34$, and decreased slightly with downstream distance, always remaining above unity. The salient parameters of the velocity field are listed in table 1.

The thermal field was produced by means of a *mandoline*, a parallel array of fine wires (Warhaft & Lumley 1978*a*), placed downstream from the grid. The (tungsten) wire diameter was 0·19 mm, giving a Reynolds number, based on the wire diameter, of 54. These wires, when either heated or unheated, had no measurable effect on the velocity field. The wire spacing was either M or $2M$, the actual configurations will be discussed below. Figure 1 shows the cross-stream profiles of r.m.s. temperature fluctuations for a case in which the mandoline was placed $2M$ from the grid with $2M$ spacing between the wires, which were orientated in the y-direction. The transverse homogeneity is good; there is less than 5 % deviation in the r.m.s. temperature across the core, which is about 7 mesh lengths wide. The variation of the transverse mean temperature was negligible. Other mandoline configurations had similar transverse homogeneity profiles.

Helium was fed into the flow through both ends of the upper set of hollow grid bars, which had holes of 0·16 cm diameter every mesh length, placed where the upper grid

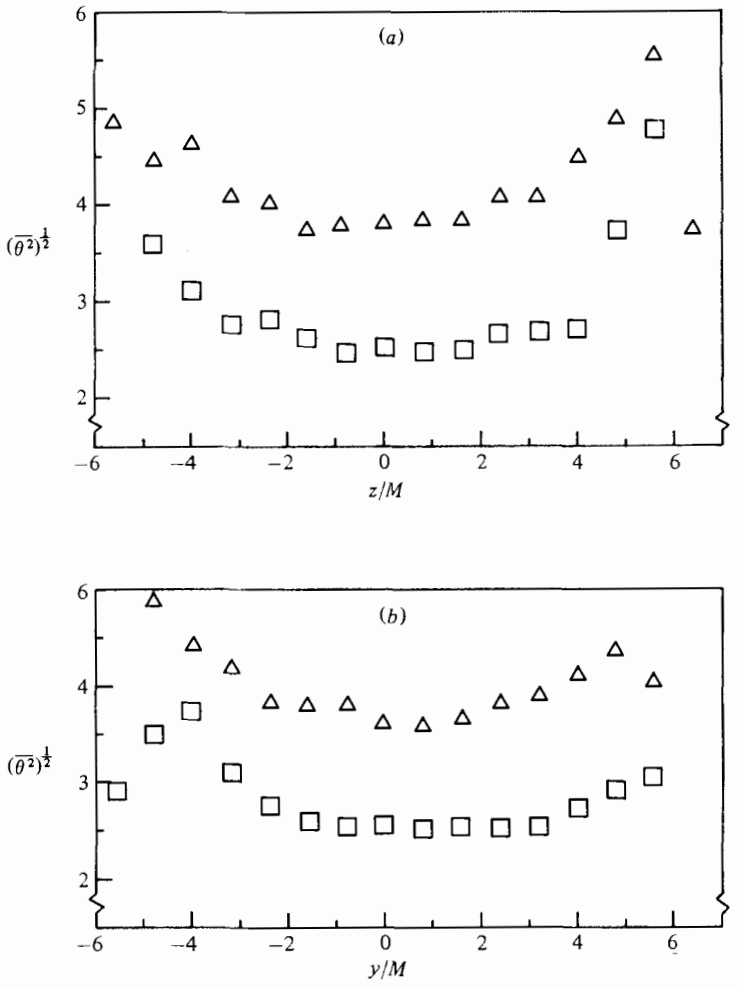

FIGURE 1. Transverse profiles of r.m.s. temperature for the mandoline (2, 2). The wires are oriented in the y-direction. △, $x/M = 34$; □, $x/M = 52$. The units for r.m.s. θ, which are the same for (a) and (b), are arbitrary.

bars crossed the lower grid bars (figure 2a). Small circular-cross-section tubes one mesh long, 0·16 cm inside diameter and 0·23 cm outside diameter were vertically positioned and soldered to the grid above the holes. These fixed tubes were used to accommodate variable-length chimneys (0·23 cm inside diameter, 0·33 cm outside diameter) which were placed over them like a collar. The chimney lengths were varied from 2 to 6 mesh lengths for the various experiments to be described below; this allowed some variation of the input scale of the helium fluctuations, and we were thus able to examine the dependence of the decay rate of helium variance $\overline{c^2}$ and the decay rate of the cross-correlation between temperature and helium fluctuations $\rho_{\theta c}$ on initial conditions.

Figure 2 shows some typical grid and mandoline arrangements. Note that in figures 2 (a, b, d) the helium is fed into the flow through chimneys $2M$ long, spaced $2M$ apart. Alternate tubes have been blocked off, and are drawn as dashed lines in the diagram. It will be shown that introducing the helium through chimneys spaced $2M$ apart, rather than M apart, changed the helium length scale, as did varying the length

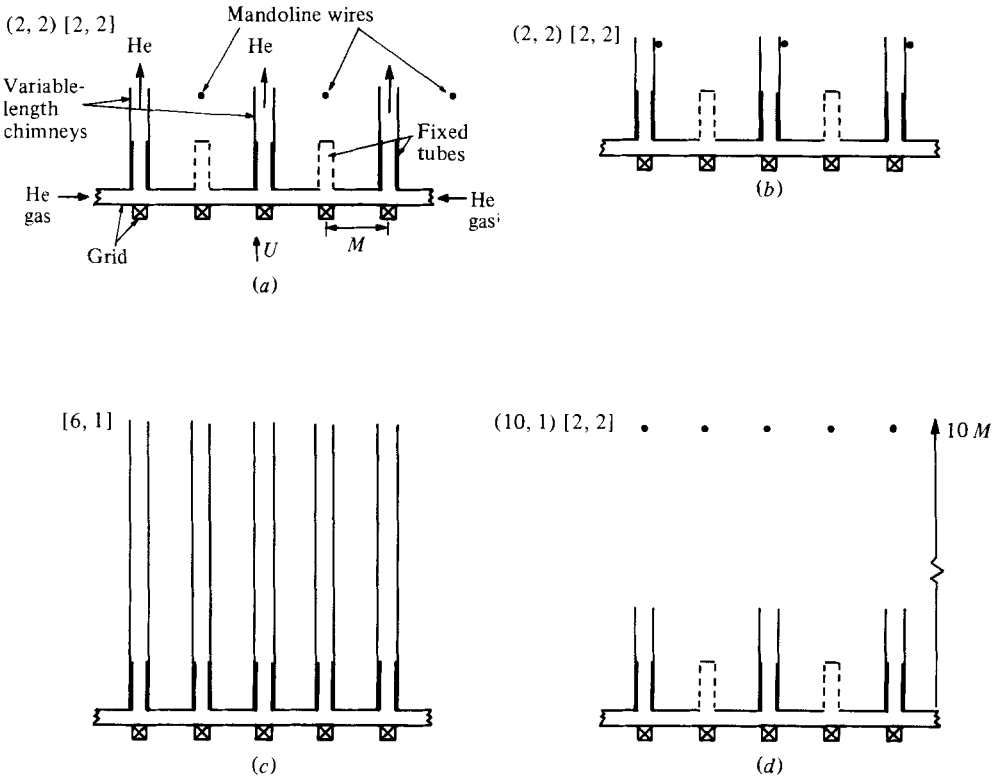

FIGURE 2. Some of the chimney and mandoline configurations. The dashed lines signify closed chimneys.

of the chimneys. Furthermore, the helium fluctuations were significantly larger when the chimneys were $2M$ apart (also transverse homogeneity was much better); thus many more measurements were carried out for this case than for the cases where the chimneys were M apart. In figure 2 and for the description to follow, the chimney configuration is described by two numbers in square brackets where the first number is the length of the chimneys and the second is their spacing, in mesh lengths. Thus [6, 1] means the chimneys are 6 mesh lengths long and are spaced one mesh length apart. This is the same notation used for the mandoline, except that square brackets rather than parentheses are used to distinguish the chimney from the mandoline configurations; (10, 1) for example means that the mandoline is placed 10 mesh lengths from the grid, and the wire spacing is 1 mesh length. Two other chimney configurations were also used, they were [6, 2] and [2, 1], and are not shown in figure 2.

Apart from providing a means of altering the helium length scale, the chimneys also straightened the incoming helium jets. However, there was less homogeneity in the transverse helium field than in the transverse thermal and velocity fields. Figure 3 shows the transverse profiles of r.m.s. concentration in both the y- and z-directions as well as the mean-concentration profile in the z-direction, the direction in which the helium was fed from both ends of the grid bars. The method of measurement of helium concentration c will be described below. The transverse homogeneity of mean concentration (figure 3a) is good, there is only a 2 % deviation from the mean. From this we calculated that production of helium fluctuations was negligible in the helium-variance

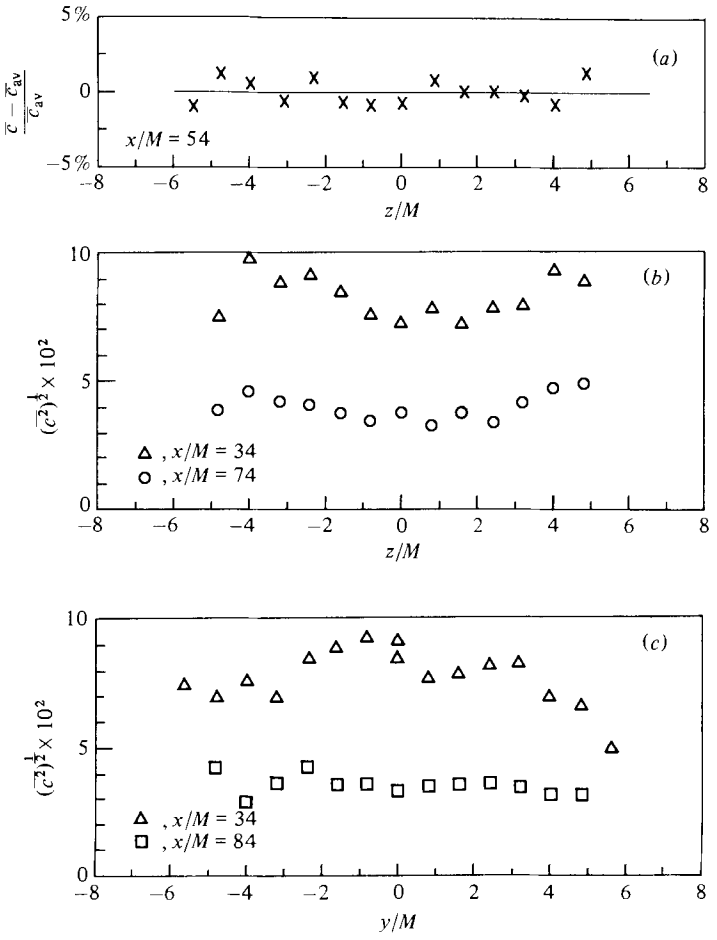

FIGURE 3. Transverse profiles for mean helium concentration (*a*) and r.m.s. helium fluctuations (*b*, *c*). The units for helium concentration are (kg He/kg mixture) × 100. The helium is fed through the grid bars along the *z*-direction.

budget, since it was less than 2 % of the dissipation term. In our preliminary tests the amount of helium entering the grid was varied until the optimum flow rate of $2{\cdot}88 \times 10^{-4}$ m^3/s per grid bar was arrived at; slower flow rates gave a helium deficit at the centre of the grid, while faster flow rates gave an enhancement. It appears that the high degree of homogeneity attained is a result of the pressure loss along the hollow grid bars due to friction being balanced by the pressure increase due to deceleration of the flow in the bars which occurs when part of the helium gas escapes from the chimneys. The transverse homogeneity of the r.m.s. helium fluctuations (figures 3*b*, *c*) is not as good as that for the temperature fluctuations (figure 1); the worst deviations are about 12 % about the mean r.m.s. value at $x/M = 34$, and this decreases with downstream distance. This departure from transverse homogeneity is comparable to that measured by Gad-El-Hak & Corrsin (1974) for their air-jet grid experiments. The co-flowing air speed of the r.m.s. profiles of figures 3 (*b*, *c*) was 3·4 m/s, lower than that used for the bulk of our measurements (4·7 m/s), although this small difference in air speed did not change the homogeneity. Considerably better homogeneity, however,

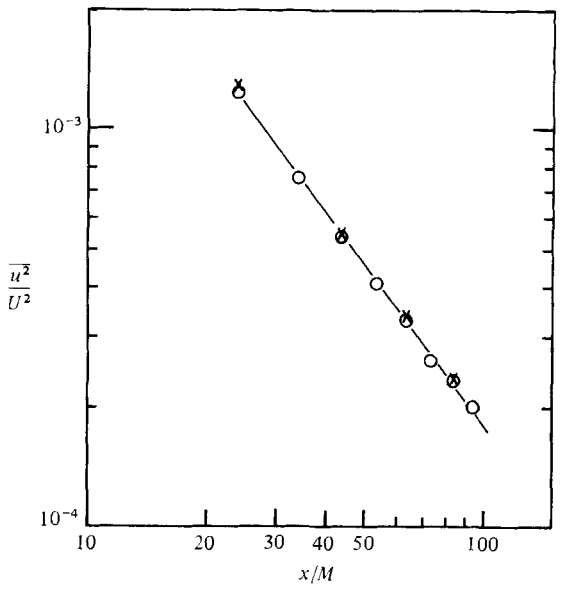

FIGURE 4. The decay of the longitudinal velocity variance. Circles are for the air only, crosses are for the addition of helium.

was obtained with faster co-flowing air speeds ($\gtrsim$ 8 m/s), but at these higher air speeds the frequency response of our helium probe was inadequate. It should be noted that the degree of transverse r.m.s. helium inhomogeneity (figures 3*b*, *c*) is too small to affect the helium variance or flux budget; simple calculations show that the third-order transport terms were negligible compared with the dissipation term in the helium-variance equation.

For all flows the total volume flow rate of helium leaving the grid was $2{\cdot}3 \times 10^{-3}$ m^3/s. The air volume flow rate passing through the grid was 0·194 m^3/s, thus the ratio of helium to air volume flow rates was 1·19 %, and the ratio of their mass flow rates was 0·164%. This very low helium volume flux (and hence mass flux) was used to ensure that helium was a passive additive. Figure 4 shows the velocity-variance decay with and without helium in the flow; there is no difference in their magnitudes. The ratio of the buoyancy term $(g/\bar{\rho})\overline{\rho u}$ to the energy-dissipation term in the energy equation was less than 1 % at $x/M = 80$. Figure 4 also shows that the chimneys did not alter the form of the law for the $\overline{u^2}$ decay; from the graph $\overline{u^2}/U^2 = 0{\cdot}0845(x/M)^{-1{\cdot}33}$ (see table 1). This compares well with velocity-variance decay laws for normal biplanar grids (e.g. Warhaft 1981).

The average speed of the helium jets entering the flow was approximately 8 m/s for configurations [6, 2] and [2, 2], and 6 m/s for configurations [6, 1] and [2, 1] (the reason that the helium jet speed for these latter cases is not half that of the cases when every other helium chimney was closed ([6, 2] and [2, 2]) is because to obtain better horizontal homogeneity for the [6, 1] and [2, 1] configurations, a number of the chimneys near the wall of the tunnel were closed). Thus for all cases studied here the speed of the incoming helium is faster than that of the co-flowing air (4·7 m/s and in some cases 5 m/s).

The mean temperature of the helium jet emerging from the chimneys was found to vary by as much as 1 °C from that of the air. However, the temperature fluctuations

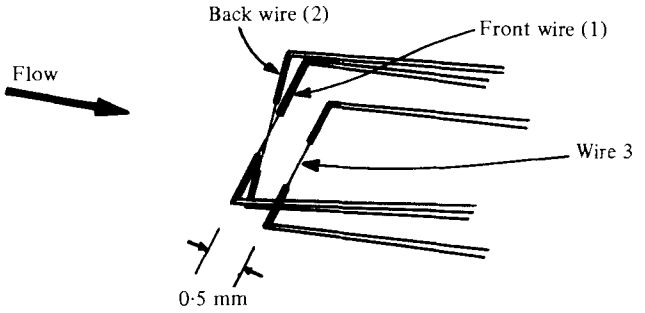

FIGURE 5. The 3-wire probe for the measurement of longitudinal velocity, helium concentration and temperature.

caused by this difference were negligible by the time the helium jets had coalesced at about $x/M = 30$ (figure 9, to be discussed below, shows a typical temperature noise spectrum).

2.2. *The 3-wire Helium–temperature–velocity probe*

Helium c, temperature θ, and longitudinal velocity u, fluctuations were measured simultaneously by means of a modified two-wire 'Way–Libby' interference probe (Way & Libby 1970, 1971; Libby 1977) that was sensitive to the u- and c-fluctuations, and a third wire placed close to the interference probe that was sensitive to u, c and θ. A sketch of the probe is shown in figure 5. The interference probe consisted of a 3 μm diameter tungsten wire with an overheat OH of 1·2 and length/diameter ratio of 100 placed approximately 5 μm in front of a 5 μm platinum–rhodium wire of $OH = 1{\cdot}6$ and $l/d = 200$. Both wires were driven from DISA type 55M constant-temperature bridges. The angle between the two wires was approximately 10°, so that a large portion of the front wire was in the thermal field of the back wire. The principle of the interference probe is that while the back wire follows King's law, the front wire does not; it is affected strongly by the variations of the thickness of the thermal field of the back wire, in which it partly resides. The thickness of the thermal field of the back wire is determined by both the variations of the velocity and the concentration field. If, for example, there is an increase in helium concentration, while the velocity field remains constant, the electrical power to the back wire must increase (in order to hold its temperature constant) owing to the higher thermal conductivity of the helium; however, the voltage of the front wire may actually decrease because it is being affected more strongly by the larger thermal field of the back wire. Thus the two wires respond differently to the presence of c and u, and by proper calibration and inversion techniques these two fields can be determined unambiguously (for more detailed discussion see Libby 1977). The actual degree of heating of the front wire by the back wire, of course, depends on their relative overheats and proximity, and because no two wires are the same the calibration characteristics vary greatly for different interference probes.

Figure 6 shows a typical calibration mesh for one of our interference probes. Note that we are only concerned with very low helium concentrations; compare figure 6 with the calibration of Stanford & Libby (1974, figure 2) for example. From this mesh (figure 6) for a given voltage pair E_1, E_2 (where E_1 is the voltage of the front wire and E_2 is the voltage from the back wire), unambiguous values of u and c may be obtained.

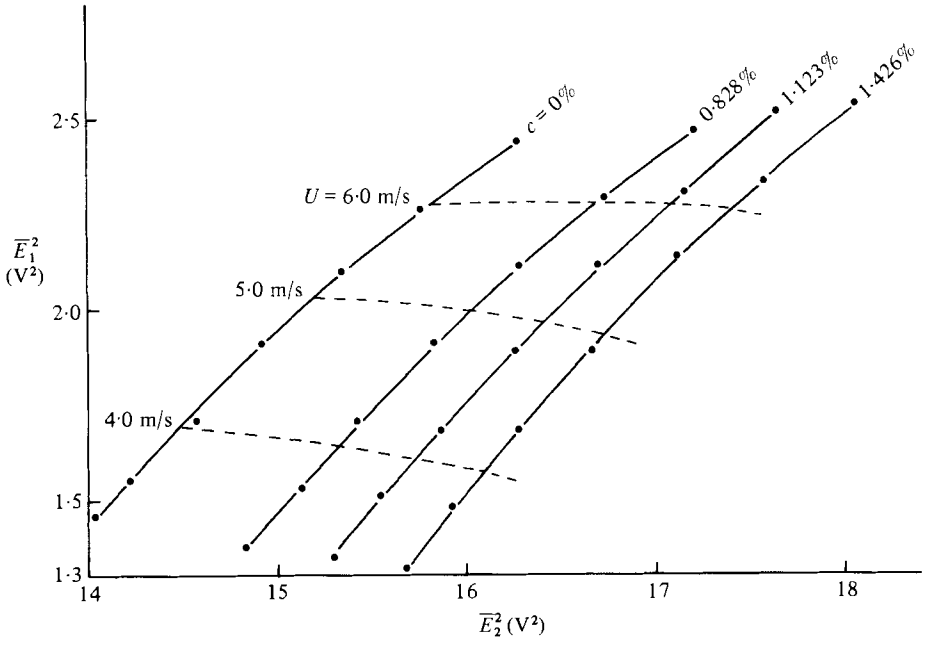

FIGURE 6. The calibration mesh for the interference probe (wires 1 and 2 of figure 5).

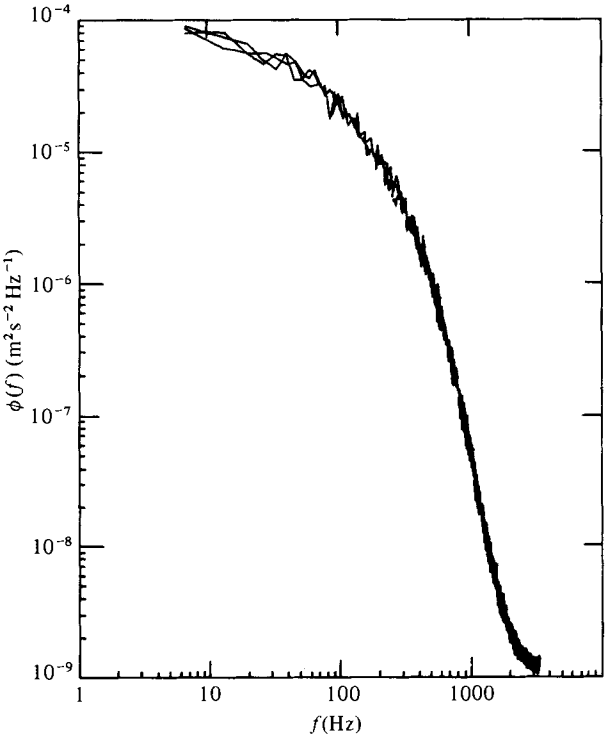

FIGURE 7. Velocity spectra derived from the interference probe. The three spectra are for air only, air with helium, and air with helium and temperature fluctuations. Their levels are within a few per cent of each other. The measurements were made at $x/M = 54$.

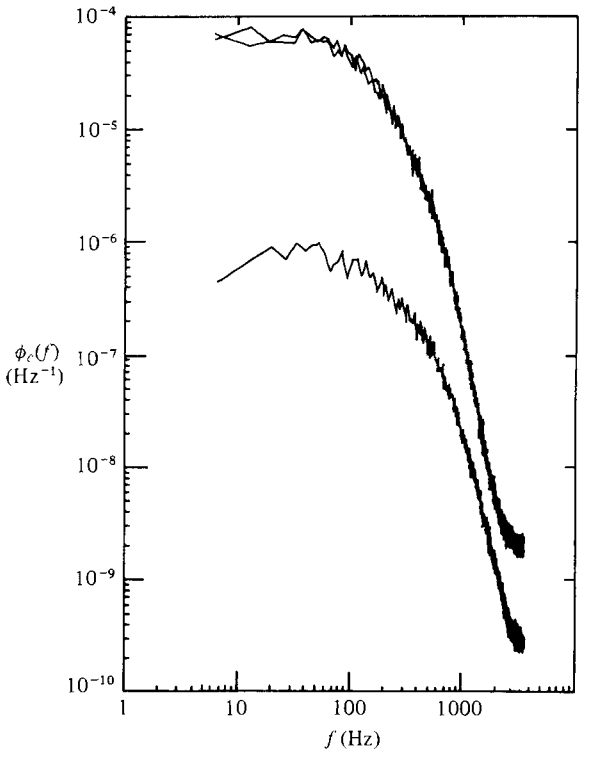

FIGURE 8. Spectra of concentration fluctuations derived from the interference probe. Lower curve is the helium noise spectrum. The two upper curves are with helium in the flow and with helium and temperature fluctuations in the flow. Their levels are within a few per cent of each other. The measurements were made at $x/M = 34$. The units of c used throughout this work are (kg He/kg mixture) × 100.

The actual details of the calibration process (in which both the helium concentration and mean velocity were varied in a calibration tunnel) are given in Sirivat (1982). The voltage pairs were inverted in the same manner as described in LaRue & Libby (1977); a preliminary inversion was also done using the method of Way & Libby (1971), and the same results were obtained. All data analysis and acquisition was done on a PDP 11/34 minicomputer.

In order to measure temperature fluctuations simultaneously with u and c a third wire was placed close (within approximately 0·5 mm) to the interference probe (figure 5). This was a tungsten wire of 3 μm diameter and $l/d = 200$, operating at a low (but not negligible) overheat of 1·05, also in a constant-temperature mode. This wire was sensitive to all three fields i.e. u, c and θ. We note that the thermal fluctuations were very weak in these experiments (approximately 0·1 °C r.m.s. maximum), and it was found that the interference probe, operating at moderate overheats, was insensitive to them. Figure 7 shows the velocity spectra derived from the interference probe without the presence of any scalar field, with He fluctuations present, and with both He and temperature fluctuations present. The level does not change with the addition of the scalars. In particular, it should be noted that the presence of the thermal field does not affect the level of the velocity spectrum, which was deduced by inverting the calibration of figure 6. The lack of interference by the θ-field on the interference

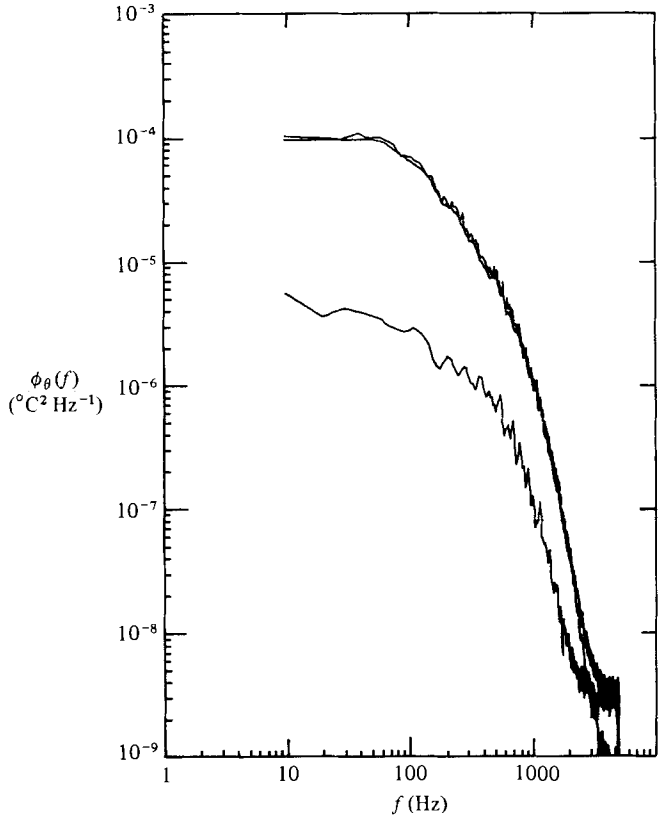

FIGURE 9. Temperature spectra derived from wire 3 (figure 5) after correcting for helium and velocity fluctuations. The lower curve is the noise spectrum, the two upper curves are the temperature spectra with and without the noise spectrum subtracted. Their levels are within a few per cent of each other.

probe is further borne out by the c-spectrum of figure 8. The two upper spectra, measured with helium only and with helium and temperature fluctuations both present, are essentially the same. The lower spectrum is the noise level for the helium fluctuations (measured with no scalar field in the flow), and its value of 0·015 % (kg He/kg mixture) compares well with the r.m.s. noise measured by Stanford & Libby (1974). Note that our inversion procedure could not erradicate some sensitivity to the velocity field, but this spectrum is nearly two decades below that of the signal in the energy-containing range (approximately 100 Hz) and about one decade below the signal in the dissipation range (approximately 1000 Hz, see §3). The overall signal-to-noise ratio $\overline{c^2}/\overline{c_n^2}$ was approximately 60/1 for this example, and did not decrease significantly with x/M. While this ratio is not high enough to deduce information about the dissipation range, it is clearly high enough for studying the energy-containing range, the subject of this enquiry.

Figure 9 shows the temperature spectrum. The temperature time series from which this was calculated was obtained from the third wire, which was sensitive to u, c and θ; i.e. the voltage from wire 3, E_3 was assumed to be of the form

$$E_3^2 = (A(c)+B(c)\ U^{0\cdot5})\ (\bar{\theta}_w-\theta), \tag{1}$$

where $A(c)$ and $B(c)$ are polynomial functions of the instantaneous He field (deduced from the interference probe), $\overline{\theta}_w$ is the wire temperature and θ is the instantaneous temperature of the medium. Equation (1) is of the same form as the equation for wire 2 of the interference probe (which also follows King's law) except that for wire 2 the last term in parentheses $(\overline{\theta}_w - \theta)$ was essentially constant because of the much higher wire overheat (for wire 2 θ_w is of the order 400° above ambient, while for wire 3 θ_w was only of the order of 10° above ambient temperature). Note that as for the c-spectrum, there is a turbulence-type noise spectrum (lower curve, figure 9) but when this was subtracted from the measured θ-spectrum it did not significantly alter its level (two upper spectra), except in the high-wavenumber region of the spectrum.

The temperature and velocity spectra measured with the 3-wire system were compared with the temperature and velocity spectra measured using conventional methods (a high-response resistance thermometer and a constant-temperature anemometer at 1·8 *OH*) in the same flow but without helium fluctuations. The levels of the spectra were the same up to about 1200 Hz, and the total temperature and velocity variances using the two different methods were within a few per cent of each other. Since the frequency response of the conventional instruments had been determined to be higher than the Kolmogorov frequency it follows that the three-wire system has an adequate frequency response to θ- and u-fluctuations. Furthermore, since the method of measuring θ and u involved all three wires, we believe that the frequency response of the system to the helium fluctuations should be comparable to that of the velocity and temperature response, since the same 3 wires were used for measuring the helium fluctuations. We note (see tables 2 and 3, §3 below) that the Kolmogorov length scale is larger for helium than for temperature, i.e. the frequency response needed to detect the helium fluctuations is less than that required for temperature and velocity.

Finally we note that our initial aim was to measure the temperature fluctuations by means of the fine platinum resistance wire (operating in a constant-current mode) used in our previous measurements (Warhaft & Lumley 1978*a*, *b*). However, preliminary measurements with the helium in the flow produced a very spiky voltage that was a strongly nonlinear function of helium concentration. The wire was also much more sensitive to the helium fluctuations than to the temperature fluctuations. Thus this approach was abandoned in favour of the constant-temperature tungsten wire described above.

3. The results

We will examine first the decay of temperature variance, and compare this with the helium-variance decay measurements. Then we will describe the heat- and concentration-flux measurements, and finally we will study the scalar-covariance measurements, comparing the direct method of injecting both helium and temperature fluctuations with the inference method, which uses temperature only.

3.1. *The scalar-variance decay*

3.1.1. *The temperature variance.* Figure 10 shows the decay of thermal variance $\overline{\theta^2}$ for 3 different mandoline configurations, and table 2 lists the various fluctuation characteristics of these flows. The decay-rate power laws (table 2) were determined

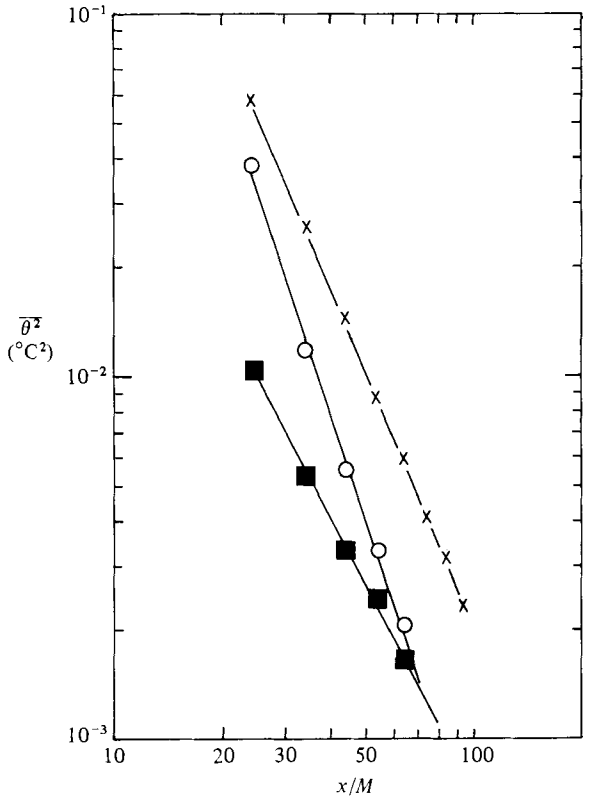

FIGURE 10. The decay of temperature variance downstream of the mandoline. ■, mandoline configuration (2, 2); ○, (10, 1); ×, (10, 2). See table 2 for values. The origin is at the grid.

by a least-squares fit to the data. The origin has been taken at the grid ($x/M = 0$); no virtual origin was needed to fix the best straight line through these data, or through the helium-variance data to be described below. The decay rates compare well with those of our previous studies for the same mandoline configurations, even though here the R_M is only 3560, compared with approximately 10000 in our previous work. It should be noted that the decay rate of $\overline{\theta^2}$ is independent of the initial value of $\overline{\theta^2}$ (Warhaft 1980, 1981) and hence of the overheat of the mandoline wires. For the approximately isotropic grid turbulence of these experiments the decay rate of $\overline{\theta^2}$ is solely a function of the ratio of the input thermal length scale to input velocity length scale; and the input thermal length scale is determined by the mandoline configuration, i.e. by the distance the mandoline is placed from the grid and by the spacing between the mandoline wires. By either moving the mandoline away from the grid or by decreasing the spacing between the mandoline wires the thermal scale is decreased relative to the velocity scale, and thus the thermal-variance decay is increased.† Thus for the mandoline at (10, 2) and at (10, 1) the decay exponent m_θ in the decay law

$$\overline{\theta^2} = A_\theta (x/M)^{-m_\theta} \tag{2}$$

† The only exception to this appears to be if the mandoline is placed very close to the grid (within one or two mesh lengths). Here the thermal length scale appears to be controlled by the velocity wakes, and the mandoline wire spacing is a less sensitive parameter in determining the thermal-variance decay rate.

Mandoline configuration	(2, 2)	(10, 2)	(10, 1)
$\overline{\theta^2} = A_\theta(x/M)^{-m_\theta}$ (°C)^2 $\begin{cases} A_\theta \\ m_\theta \end{cases}$	3·624 1·84	102 2·34	440 2·95
$r_\theta = m_\theta/n$	1·38	1·76	2·22
$\epsilon_\theta = -\frac{1}{2}\frac{d\overline{\theta^2}}{dt}$ (°C^2/s)	$1{\cdot}51 \times 10^{-2}$	$7{\cdot}34 \times 10^{-3}$	$3{\cdot}50 \times 10^{-2}$
$\overline{\theta^2}$ (°C)^2 (from decay law)	$2{\cdot}35 \times 10^{-3}$	$9{\cdot}01 \times 10^{-3}$	$3{\cdot}41 \times 10^{-3}$
l/r_θ (m)	$5{\cdot}02 \times 10^{-3}$	$3{\cdot}94 \times 10^{-3}$	$3{\cdot}12 \times 10^{-3}$
k_θ (from 3-dimensional spectrum) (m^{-1})	175	200	230
$(\overline{\theta^2})_k = \epsilon_\theta(\nu/\epsilon)^{\frac{1}{2}}$ (°C^2)	$1{\cdot}71 \times 10^{-4}$	$8{\cdot}32 \times 10^{-4}$	$3{\cdot}97 \times 10^{-4}$
$\eta_\theta = \frac{1}{k_k}\left(\frac{1}{Pr}\right)^{\frac{1}{2}}$ (m)	$5{\cdot}06 \times 10^{-4}$	$5{\cdot}06 \times 10^{-4}$	$5{\cdot}06 \times 10^{-4}$

TABLE 2. Temperature field parameters for the various mandoline configurations. $\overline{U}$ = 4·7 m/s, Prandtl number $Pr = \nu/\kappa = 0{\cdot}73$, where κ is the thermal diffusivity. Fluctuation parameters were calculated for $x/M = 54$.

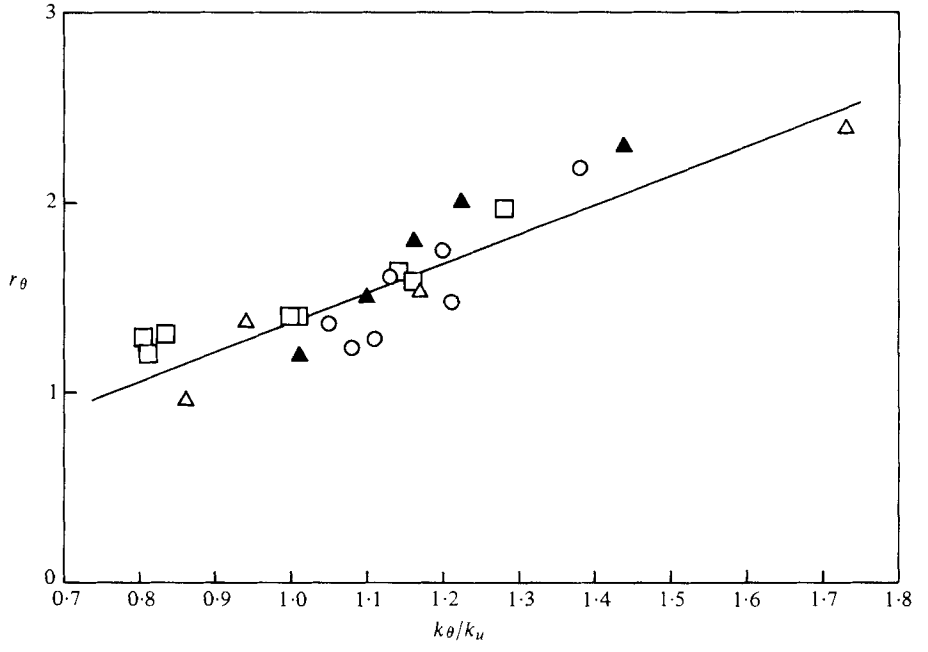

FIGURE 11. The thermal time-scale ratio r_θ *vs.* the wavenumber peak of the temperature spectrum divided by the wavenumber peak of the velocity spectrum at $x/M = 54$. △, Warhaft & Lumley (1978*a*); ▲, Warhaft (1980); □, ○, present work, with and without helium in the flow respectively.

varies from 2·34 to 2·95 (figure 10), even though the mandoline is the same distance from the grid in both cases. This is because the wavenumber of the peak in the temperature spectrum is higher for (10, 1) than for (10, 2) since the mandoline wires are closer together. On the other hand, keeping the mandoline wire spacing fixed but moving the mandoline away from the grid also increases the wavenumber at which the thermal fluctuations are introduced relative to the velocity wavenumber, since

the velocity scale grows with downstream distance although the thermal input scale is fixed for this case. Thus the decay rate for (10, 2) is greater than for (2, 2) (figure 10).†

Figure 11 shows a compilation of the present work and all the previous experiments of $\overline{\theta^2}$ decay we have so far conducted in different wind tunnels and at various Reynolds and Péclét numbers (Warhaft & Lumley 1978*a*; Warhaft 1980). Although there is some scatter, it is clear that the time-scale ratio

$$r_\theta \equiv (\overline{q^2}/\epsilon)/(\overline{\theta^2}/\epsilon_\theta), \tag{3}$$

where $\overline{q^2}$ is twice the turbulence kinetic energy, and ϵ and ϵ_θ are the destruction rates of turbulence kinetic energy and temperature variance respectively, is a monotonic function of k_θ/k_u, the ratio of the velocity length scale to the thermal length scale. Whether r_θ (which is equal to m_θ/n from the power-law decays of $\overline{\theta^2}$ and $\overline{u^2}$, Warhaft & Lumley 1978*a*) is a *linear* function of k_θ/k_u is still not clear, since there is too much scatter in the data to determine the precise functional relationship.

3.1.2. *The helium variance.* Figure 12 shows the decay of helium variance $\overline{c^2}$ for four different chimney configurations, and table 3 lists the various fluctuation characteristics for these four flows. (Figure 2 shows the chimney configurations for the flows [2, 2] and [6, 1]; configurations [6, 2] and [2, 1] are not sketched.) As for the mandoline experiments the decay rate of $\overline{c^2}$ is a function of initial conditions; m_c, the decay exponent in the law

$$\overline{c^2} = A_c(x/M)^{-m_c}, \tag{4}$$

varies from 1.47 (chimney configuration [2, 1]) to 2·84 (chimney configuration [6, 1]).‡

† In a recent paper Sreenivasan *et al.* (1980) report results that suggest the decay rate of $\overline{\theta^2}$ is independent of mandoline- (screen in their terminology) wire spacing and the distance of the mandoline from the grid; results that appear to be in conflict with those reported here and in our previous work. However, Sreenivasan *et al.* placed their screen (which was a square-mesh configuration) very far downstream ($x/M \geqslant 20$), and their wire spacing was always less than 1M. Thus in all of their work the input thermal length scale is much smaller than the velocity length scale. At these small scales their results suggest that the $\overline{\theta^2}$ decay rate has reduced sensitivity to its input conditions. In our work the mandoline has been placed $x/M \leqslant 20$ from the grid, and the thermal length scale has been varied from approximately equal to that of the velocity scale to approximately one-third the velocity scale; here the sensitivity of the $\overline{\theta^2}$ decay to input conditions is clearly evident. This difference between the initial conditions used in our work and in the work of Sreenivasan *et al.* has been further borne out by a recent investigation of scalar variance decay by Durbin (1981), using a Lagrangian dispersion theory. We note also that plotting our data using the mandoline as the origin (rather than the grid), as Sreenivasan *et al.* do, still preserves the variation in our $\overline{\theta^2}$ decay; decreasing the input thermal scale is still associated with an increase in the $\overline{\theta^2}$ decay rate. Furthermore, we find that using the mandoline as the origin can result in ambiguity. For example in Warhaft (1981) it has been shown that the same input thermal scale may be achieved if the mandoline is at (10, 1) or at (15, 2). The effect of moving the mandoline away from the grid (decreasing the length scale) has been exactly compensated by increasing the distance between the mandoline wires (which has the effect of increasing the length scale). For both these cases the same decay rate of $\overline{\theta^2}$ is observed if the data is plotted from the grid. If the data were plotted from the mandoline, different decay laws would result for the same thermal length scale.

‡ For the case [6, 1] the helium field became inhomogeneous at approximately $x/M = 60$, and thus we have no evidence for the decay beyond this point. The reason this flow became inhomogeneous was that a number of chimneys near the wall were blocked off to produce transverse homogeneity at the initial stages of the flow (§2.1), this, however, caused a much larger helium boundary layer, and the core became intolerably small because of this after $x/M = 60$.

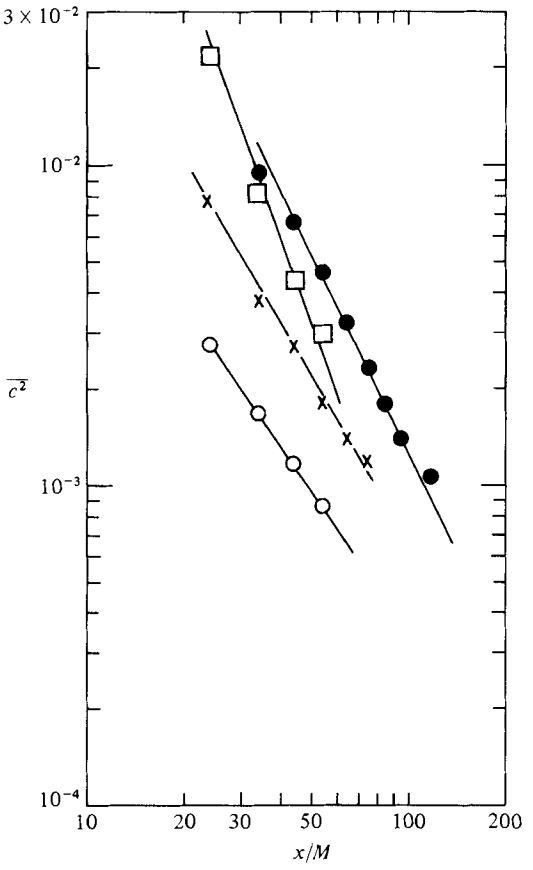

FIGURE 12. The decay of helium variance downstream of the chimneys. ○, chimney configuration [2, 1]; ×, [2, 2]; □, [6, 1]; ●, [6, 2]. See table 3 for values. The origin is at the grid.

Figure 13 shows the 3-dimensional spectra of the helium fluctuations at $x/M = 54$, and as for the mandoline experiments, it is evident that there is a definite correspondence between the $\overline{c^2}$ decay rate and the scale of the helium fluctuations, i.e. smaller scales are positively correlated with faster variance decay rates. Note that for the case [2, 1] the helium scale is slightly larger than for the case [2, 2] (figure 13), a result contrary to expectation, which would have suggested that [2, 2] would have produced a larger scale since the chimneys are further apart (cf. the cases [6, 1] and [6, 2]). However, the positive correlation between faster decay rate and smaller input scale is still preserved: m_c for the case [2, 2] is greater than for the case [2, 1] (table 3), in keeping with the smaller scale for the former case.

Because of difficulties in measurement of the helium fluctuations, and the greater inhomogeneity of the helium field compared with that of the thermal field, we carried out a number of $\overline{c^2}$ decay measurements for each chimney configuration over the many months of the experimental programme. Various probes were used with different calibrations, and for each experiment the flow conditions and homogeneity in the helium field were found to vary. Figure 14 is a summary of these experiments. The ordinate is the helium time-scale ratio defined as

$$r_c \equiv (\overline{q^2}/\epsilon)/(\overline{c^2}/\epsilon_c), \tag{5}$$

Chimney configuration	[2, 1]	[2, 2]	[6, 2]	[6, 1]
$\bar{U}$ (m/s)	5	4·7	4·7	5·0
$\overline{c^2} = A_c(x/M)^{-m_c}$ A_c	0·299	1·63	16·02	210·0
m_c	1·47	1·69	2·05	2·84
$r_c = m_c/n$	1·11	1·27	1·54	2·14
$\epsilon_c = -\frac{1}{2}\frac{d\overline{c^2}}{dt}$ (s^{-1})	$4{\cdot}62 \times 10^{-3}$	$1{\cdot}13 \times 10^{-2}$	$3{\cdot}21 \times 10^{-2}$	$2{\cdot}64 \times 10^{-2}$
$\overline{c^2}$ (from decay law)	$8{\cdot}49 \times 10^{-4}$	$1{\cdot}93 \times 10^{-3}$	$4{\cdot}50 \times 10^{-3}$	$2{\cdot}53 \times 10^{-3}$
l/r_c (m)	$6{\cdot}24 \times 10^{-3}$	$5{\cdot}46 \times 10^{-3}$	$4{\cdot}50 \times 10^{-3}$	$3{\cdot}24 \times 10^{-3}$
k_c (from 3-dimensional spectrum) (m^{-1})	126	130	152	190
$(\overline{c^2})_k = \epsilon_c(\nu/\epsilon)^{\frac{1}{2}}$	$5{\cdot}22 \times 10^{-5}$	$1{\cdot}28 \times 10^{-4}$	$3{\cdot}64 \times 10^{-4}$	$2{\cdot}98 \times 10^{-4}$
$\eta_c = \frac{1}{k_k}\left(\frac{1}{Sc}\right)^{\frac{1}{2}}$ (m)	$8{\cdot}67 \times 10^{-4}$	$9{\cdot}02 \times 10^{-4}$	$9{\cdot}02 \times 10^{-4}$	$8{\cdot}67 \times 10^{-4}$

TABLE 3. Helium field parameters for various chimney configurations. Schmidt number $Sc = \nu/D = 0{\cdot}23$, where D is the helium diffusivity in air. Units for c are (kg He/kg mixture) $\times 100$. Fluctuation parameters were calculated for $x/M = 54$.

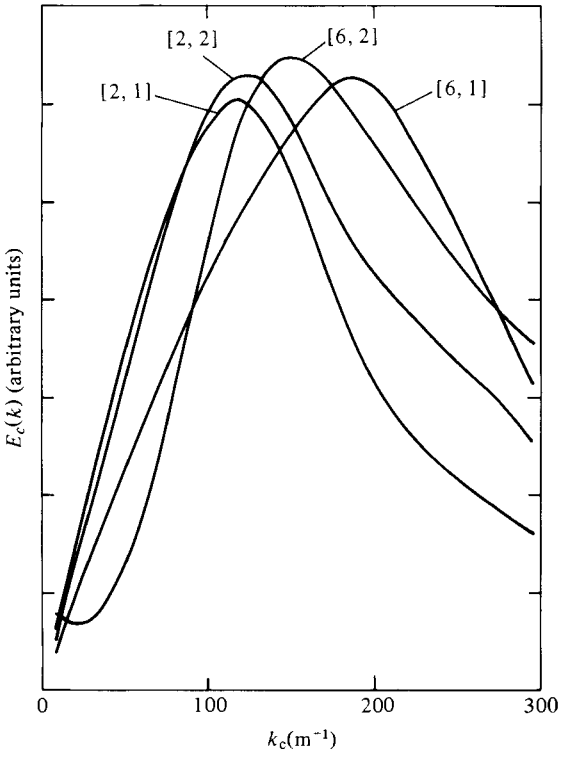

FIGURE 13. The three-dimensional helium spectra at $x/M = 54$ for the four helium variance decay experiments of figure 12.

where ϵ_c is the dissipation rate of helium variance. $r_c = m_c/n$ since $\overline{c^2}$ follows a power-law decay. The abscissa is the ratio of the peak in the 3-dimensional helium spectrum to that of the 3-dimensional velocity spectrum. Although there is scatter for reasons mentioned above, it is clear from this plot that as for the temperature variance, r_c is approximately proportional to k_c/k_u. The solid line is the line of best fit to these data

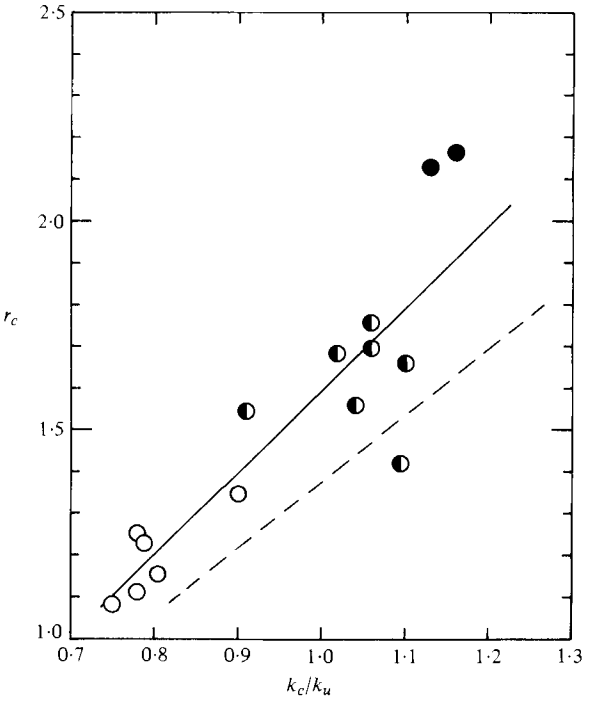

FIGURE 14. The helium time-scale ratio r_c *vs.* the wavenumber peak of the helium spectrum divided by the wavenumber peak of the velocity spectrum at $x/M = 54$. ●, chimney configuration [6, 1]; ◐, [6, 2]; ○, [2, 2] and [2, 1]. The dashed line is the line of best fit for r_θ, from figure 11.

points. The dashed line is the line of best fit for all our thermal-variance decay measurements (figure 11). The line for the temperature measurements falls below that of the helium measurements, showing that for a given scalar time scale ratio, the helium length scale is larger than the thermal length scale. We note that by definition, the helium Taylor microscale λ_c is larger than the temperature Taylor microscale λ_θ when $r_c = r_\theta$. This may be shown by substituting the formal definitions

$$\epsilon_\theta = 6\kappa\overline{\theta^2}/\lambda_\theta^2, \quad \epsilon_c = 6D\overline{c^2}/\lambda_c^2 \tag{6}$$

into the definitions of r_θ and r_c, (3) and (5). The equation

$$r_\theta/r_c = (\kappa/D)\,\lambda_c^2/\lambda_\theta^2 = 0{\cdot}31\,\lambda_c^2/\lambda_\theta^2 \tag{7}$$

results. For $r_\theta = r_c$, $\lambda_c = 1{\cdot}8\lambda_\theta$. The larger value for the helium integral scale (figure 14) for $r_\theta = r_c$ is thus consistent with the larger value of the Taylor microscale for the helium fluctuations, although from a theoretical viewpoint it is not clear how these two scales should be related for scalars. Whether the departure from the parallel of the r_c and r_θ line in figure 14 is of significance or is due to experimental scatter is also unclear.

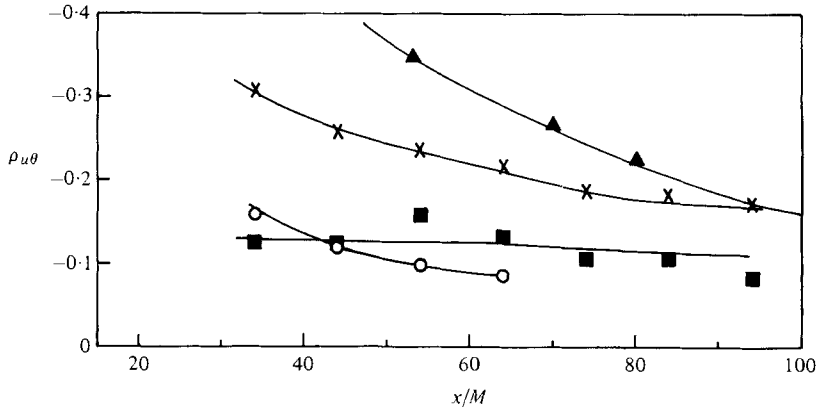

FIGURE 15. The decay of the cross-correlation between u and θ. ■, mandoline configuration (2, 2); ○, (10, 1); ×, (10, 2); ▲, (20, 1) (the top curve is taken from Warhaft & Lumley 1978*b*).

3.2. *Heat- and mass-flux decay*

The decay of scalar variance $\overline{\theta^2}$ and $\overline{c^2}$, described above, is due to the destruction of the scalar fluctuations by the action of molecular dissipation. The governing equations are†

$$\frac{d\overline{\theta^2}}{dt} = -2\kappa \overline{\frac{\partial\theta}{\partial x_j}\frac{\partial\theta}{\partial x_j}}, \tag{8}$$

$$\frac{d\overline{c^2}}{dt} = -2D \overline{\frac{\partial c}{\partial x_j}\frac{\partial c}{\partial x_j}}. \tag{9}$$

If the input scalar field is by some means correlated with the velocity field then a flux $\overline{u\theta}$ or $\overline{uc}$ will exist, and this too could be expected to decay. The existence of a scalar flux represents anisotropy in the scalar field, and the decay of the flux is due to the return to isotropy of the scalar field. Thus the mechanism for the decay of the scalar flux is quite different from that of the decay of scalar variance. It is governed by the equations

$$\frac{d\overline{u\theta}}{dt} = -\frac{1}{\rho}\overline{\theta\frac{\partial p}{\partial x_i}} - (\nu+\kappa)\overline{\frac{\partial\theta}{\partial x_j}\frac{\partial u_i}{\partial x_j}}, \tag{10}$$

$$\frac{d\overline{uc}}{dt} = -\frac{1}{\rho}\overline{c\frac{\partial p}{\partial x_i}} - (\nu+D)\overline{\frac{\partial c}{\partial x_j}\frac{\partial u_i}{\partial x_j}}. \tag{11}$$

Since in locally isotropic turbulence the molecular transport terms on the right-hand sides of (10) and (11) are negligible, the rate of change of the scalar flux is due solely to the scalar–pressure derivative correlation, which effects the return to isotropy.

3.2.1. *The heat-flux correlation coefficient.* Figure 15 shows measurements of the decay of $\rho_{u\theta}(\equiv \overline{(u\theta)}/(\overline{u^2}\,\overline{\theta^2})^{\frac{1}{2}})$, the cross-correlation of u and θ. We will use $\rho_{u\theta}$, rather than $\overline{u\theta}$, since the correlation coefficients facilitate better comparison of results. The results shown are for the measurements done in the present tunnel as well as for those done previously in a tunnel of larger cross-section (Warhaft & Lumley 1978*b*). All are for heated mandolines placed at various distances from the grid. The flux is produced

† Turbulent production and transport terms have been neglected in these equations, and (10)–(12) and (15) to follow, since our flows were approximately homogeneous (§2), and these terms account for only a few per cent of the variance, covariance and flux budgets.

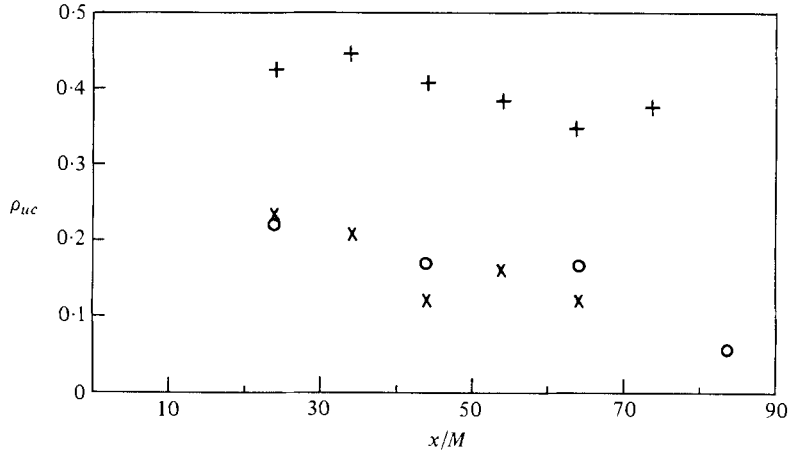

FIGURE 16. The decay of the cross-correlation between u and c. The three trials are all for the chimney configuration [2, 2].

by increasing the current in the mandoline; the mechanism of flux production is thought to be due to the slight velocity deficit (produced by the mandoline), which causes a negative cross-correlation between u and θ but is too small to effect the velocity field, although the mechanism suggested in Warhaft (1980) may also play a role.

Figure 15 shows that the decay rate of $\rho_{u\theta}$ is a function of the mandoline configuration, i.e. the scale of the thermal fluctuations relative to the velocity scale. Thus for (20, 1) the return to isotropy is faster than for (10, 2), and for (2, 2) $\rho_{u\theta}$ hardly decays at all. This latter situation, where the mandoline is placed very close to the grid and thus is directly in the wake of the grid bars is quite similar to the decay of $\rho_{u\theta}$ for heated-grid experiments (e.g. Warhaft & Lumley 1978*a*, figure 19), where it is also found that $\rho_{u\theta}$ decays very slowly, if at all.

It appears that if the scalar is injected at, or close to, the grid it hardly forgets its mode of generation, and remains forever coupled to the velocity field, and there is no return to isotropy. Note that for this case $r_\theta \sim 1$, and the thermal and velocity length scales are approximately the same. However, if the scalar flux is introduced into the flow far downstream where the velocity wakes have coalesced and the velocity field is approximately isotropic, then the $\rho_{u\theta}$ decays, and there is a return to isotropy of the scalar field. Here the length scale of the thermal field is determined independently of the velocity field, unlike the case when the scalar is injected close to the grid.

The case in which the flux is produced far downstream of the grid is amenable to theoretical treatment, since the turbulent field is isotropic. For this case Lumley (1978) has successfully applied second-order modelling procedures to estimate the rate of return to isotropy. For the heated-grid case, and for the mandoline placed close to the grid, the heat flux is formed in a strongly anisotropic flow, and the large-scale coherence produced by the grid-bar wakes makes this problem less amenable to the theoretical treatment, although it should be of considerable interest since it shows that under these conditions there is virtually no return to isotropy of the thermal field.

3.2.2. *The helium flux.* For the cases where the helium chimneys were placed two mesh lengths apart the speed of the incoming helium gas was significantly higher than that of the co-flowing air (§2), and thus a positive cross-correlation between u and c

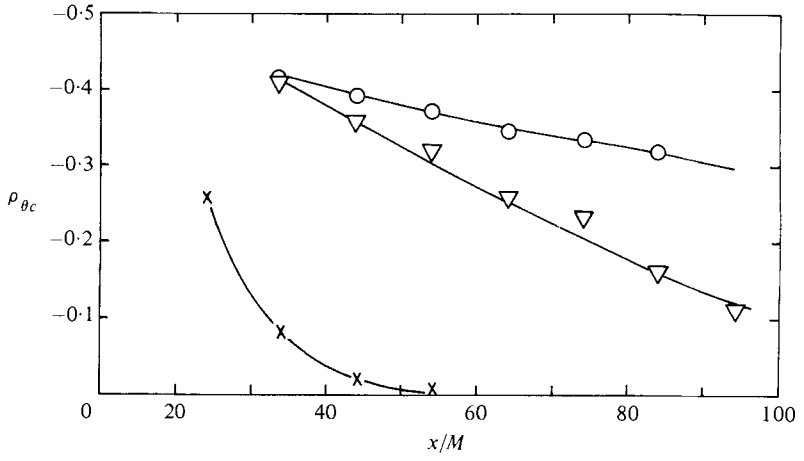

FIGURE 17. The decay of the cross correlation between θ and c. ×, mandoline and chimney configurations (10, 1), [2, 2]; ▽, (10, 2), [2, 2]; ○, (2, 2), [2, 2].

would be expected. Figure 16 shows ρ_{uc} for the chimney configuration [2, 2] for three slightly different helium injection speeds (but in all cases with the helium velocity greater than the air velocity). Here, as for the mandoline at (2, 2), the decay of ρ_{uc} is slow, i.e. the grid-bar wakes appear to cause a strong coupling of the helium field to the velocity field, and this coupling remains for the flow duration. Note also that here the helium flux is positive, as opposed to the heat flux, which was negative, but there is little qualitative difference in the nature of the cross-correlation decay for the two cases.

Unfortunately we were unable to examine a case for helium-flux decay in which the helium was fed into the flow at a smaller scale than the velocity field. For the chimney configuration [6, 1] the speed of the incoming helium gas was approximately the same as that of the co-flowing air, and a cross-correlation between the two fields could not be determined with any accuracy. We were unable to alter the relative speeds of the helium and air for this case by a significant amount because of problems in maintaining transverse homogeneity in the helium field.

3.3. *The scalar-covariance decay*

The rate equation for the decay of scalar covariance in the absence of any production mechanism is

$$\frac{d\overline{\theta c}}{dt} = -(\kappa + D)\,\overline{\frac{\partial \theta}{\partial x_j}\frac{\partial c}{\partial x_j}}. \tag{12}$$

Here, as for the decay of the individual variances, the covariance is destroyed by the action of molecular dissipation.

In Warhaft (1981) an inference method (involving a single scalar injected into the flow at two different downstream locations) was used to determine scalar-covariance decay. Here we will first describe the direct method of measuring scalar-covariance decay by injecting the two different scalars, helium and temperature, into the flow, and then we will compare this method with the inference method.

Figure 17 shows the $\rho_{\theta c}$ decay for three different mandoline and chimney configurations. Sketches of configurations (2, 2), [2, 2] and (10, 1), [2, 2] are shown in

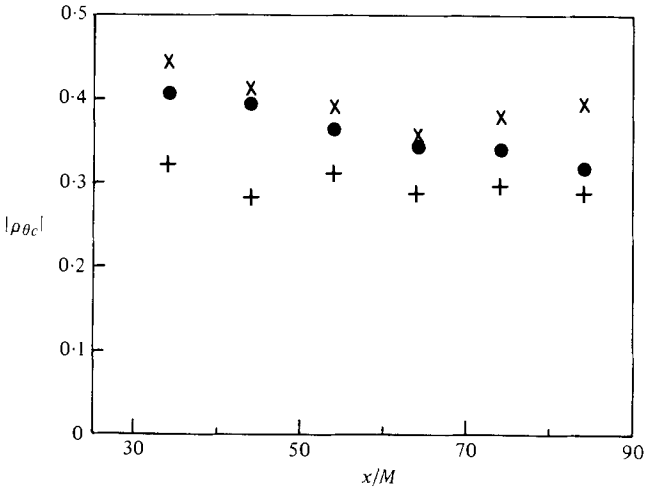

FIGURE 18. Comparison of $\rho_{\theta c}$ as a function of x/M for both positive and negative initial values. The mandoline–chimney configuration is (2, 2), [2, 2] for all cases. ●, $\rho_{\theta c}$ is negative (mandoline–chimney configuration of figure 2*a*); × and +, $\rho_{\theta c}$ is positive (two different trials, mandoline–chimney configuration of figure 2*b*).

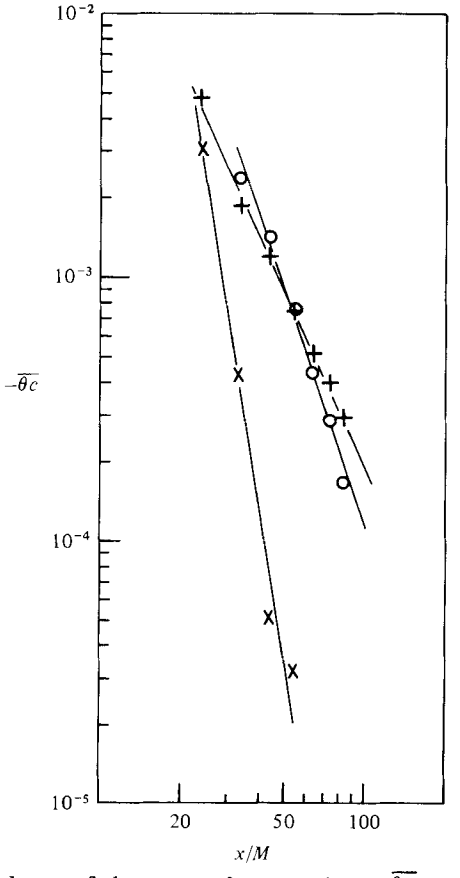

FIGURE 19. The decay of the two-scalar covariance $\overline{\theta c}$. ×, mandoline and chimney configurations (10, 1), [2, 2]; +, (2, 2), [2, 2]; ○, (10, 2), [2, 2].

figures 2(*a*, *d*) respectively. The (10, 2), [2, 2] configuration is the same as (2, 2), [2, 2] but the mandoline has been moved to 10 mesh lengths from the grid, with the wires still in the same lateral position with respect to the chimneys as in (2, 2), [2, 2] of figure 2 (*a*), i.e. they are displaced one mesh length in the transverse direction with respect to the chimneys. As for the $\rho_{u\theta}$ decay (figure 15), figure 17 shows that the decay of the scalar cross-correlation is slow if both scalars are introduced close to the grid, (2, 2), [2, 2], but the decay is rapid if there is a significant mismatch in the scales of the two scalars, i.e. if one scalar is introduced close to the grid and the other is introduced further downstream, at a much smaller scale, cases (10, 1), [2, 2]. The case (10, 2), [2, 2] is intermediate between the above two cases; here the thermal length scale is not as different from the helium length scale as for the case (10, 1), [2, 2]. (Figure 10 shows that for (10, 1) the decay rate of $\overline{\theta^2}$ is much more rapid than for (10, 2), indicating a much smaller length scale for the former case, see also table 2.) Note that for these three experiments $\rho_{\theta c}$ is negative, as could be expected from the relative positions between the chimneys and mandolines, i.e. there is generally a helium deficit where there is an enhancement in temperature. (This is clearly the case for (2, 2), [2, 2] (figure 2*a*) and for the case (10, 2), [2, 2]; for the case (10, 1), [2, 2] (figure 2*d*) the situation is less clear since some mandoline wires are directly above the chimneys and others are in regions of depleted helium.)

Other mandoline and chimney configurations were also tried (Sirivat 1982), and these tended to confirm the trends shown in figure 17, although we were unable to produce as high initial cross-correlations as shown in figure 17.

In order to determine whether the decay rate of $\rho_{\theta c}$ was a function of the sign of the initial $\rho_{\theta c}$, the mandoline was moved to the position shown in figure 2(*b*), i.e. it was still at (2, 2) but was moved one mesh laterally so that it was very close to (but not touching) the chimneys. Figure 18 shows that for this configuration $\rho_{\theta c}$ was positive, as would be expected; however, its (slow) decay rate was similar to that for the configuration (2, 2), [2, 2] shown in figure 2 (*a*), where the negative correlation was observed. Two different trials for the positive $\rho_{\theta c}$ are also shown in figure 18, and these indicate that the decay rate appears to be independent of the initial magnitude of the cross-correlation, for the small variation in the initial value of $\rho_{\theta c}$ that we were able to attain.

Figure 19 shows a plot on log–log co-ordinates of the $\overline{\theta c}$ decay, and here we see that in accordance with the cross-correlation coefficient the decay rate of $\overline{\theta c}$ is slow when the two scalars are injected close to the grid, (2, 2), [2, 2], while if there is a strong mismatch in their input scales the covariance decay rate is fast, (10, 1), [2, 2]; the exponent $m_{\theta c}$ in the decay law

$$\overline{\theta c} \propto (x/M)^{-m_{\theta c}} \tag{13}$$

varying from 2·2 to 5·9 for the two respective cases.

3.4. *Comparison of the direct method of measurement of scalar covariance decay with the inference method*

Warhaft (1981) showed that by placing two mandolines at different longitudinal downstream positions from a grid that the decay of scalar covariance could be inferred. The sum of the thermal variances produced by each mandoline operating separately, $\overline{\theta_1^2}+\overline{\theta_2^2}$, was found to be significantly less than the total variance produced by both mandolines operating simultaneously:

$$\overline{\theta_{\mathrm{T}}^2} = \overline{(\theta_1+\theta_2)^2} = \overline{\theta_1^2}+\overline{\theta_1^2}+2\overline{\theta_1\theta_2}, \tag{14}$$

i.e. the deficit was due to the covariance term $2\overline{\theta_1\theta_2}$. The decay of $\overline{\theta_1\theta_2}$ and

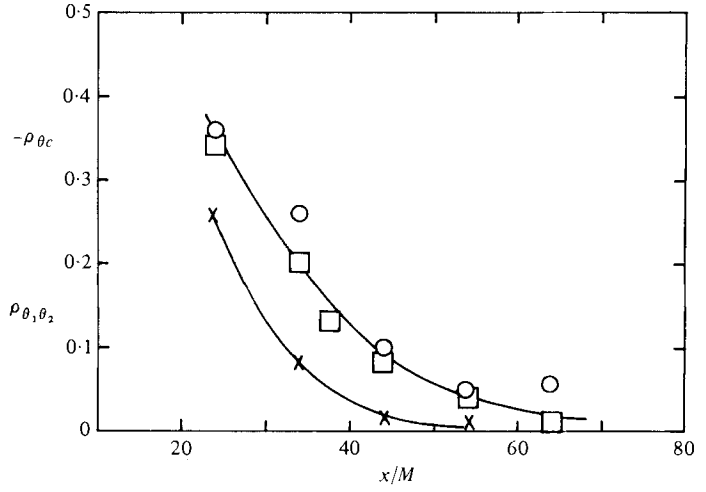

FIGURE 20. Comparison of the two-scalar covariance decay using the direct method ($\rho_{\theta c}$) and the inference method ($\rho_{\theta_1\theta_2}$). ×, mandoline and chimney configuration (10, 1), [2, 2] (from figure 17); ○, mandolines at (10, 1), (2, 2), present work; □, mandolines at (10, 1), (1.5, 2) from Warhaft (1981).

$\rho_{\theta_1\theta_2}$ ($\equiv \overline{\theta_1\theta_2}/(\overline{\theta_1^2}\overline{\theta_2^2})^{\frac{1}{2}}$) was studied for various input thermal scale sizes and for various input locations.

For the inference case the governing equation is

$$\frac{d\overline{\theta_1\theta_2}}{dt} = -2\kappa \frac{\partial\overline{\theta_1}}{\partial x_j}\frac{\partial\overline{\theta_2}}{\partial x_j}, \tag{15}$$

while for the direct method described above (§3.3) the governing relation is (12), i.e. the form of the equations is the same but the coefficients differ by a factor of two since $\kappa + D = 9{\cdot}56 \times 10^{-5}$ m^2/s, (12), and $2\kappa = 4{\cdot}52 \times 10^{-5}$ m^2/s, (15). Because κ and D are of the same order, we expect the destruction mechanisms of the scalar covariances $\overline{\theta c}$ and $\overline{\theta_1\theta_2}$ to be similar; significant differences in scalar-covariance dissipation should only become apparent if the two diffusivities differ by an order or greater, such as for the case of salinity and heat in water.

Figure 20 shows the decay of $\rho_{\theta_1\theta_2}$ for the case (10, 1), (2, 2) using the inference method, compared with the direct method for the case (10, 1), [2, 2] taken from figure 17. There is extremely good agreement between the two different methods for which the input conditions are similar. Also plotted on figure 20 is the decay of $\rho_{\theta_1\theta_2}$ for the same mandoline configurations taken from the work of Warhaft (1981), which was done in a tunnel of four times the cross-sectional area. We see that there is no difference in the $\rho_{\theta_1\theta_2}$ decay, indicating that this quantity is independent of Reynolds number for the moderate Reynolds-number variation (3560 and 10000) investigated. For the inference method the decay exponent for $\overline{\theta_1\theta_2}$ was $-5{\cdot}5$ (Warhaft 1981), while for the direct method the decay exponent for $\overline{\theta c}$ was $-5{\cdot}9$ (figure 19), again showing good agreement between the two methods.

For all the inference experiments reported in Warhaft (1981) the two mandolines were placed at different longitudinal positions from the grid, whereas for the direct measurements we have described above there were some experiments in which both scalars were fed into the flow at the same distance from the grid, i.e. the mandoline

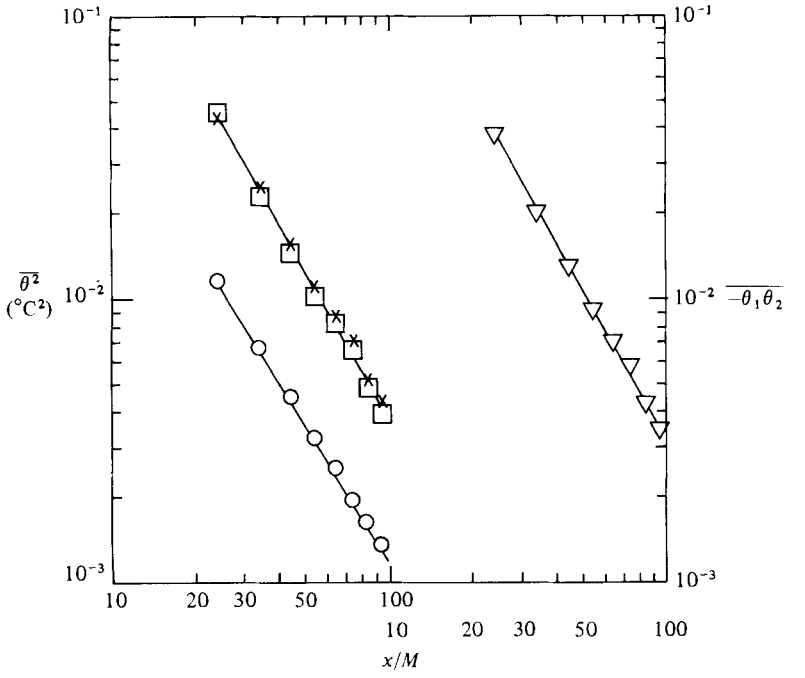

FIGURE 21. $\overline{\theta^2}$ decay and $\overline{\theta_1\theta_2}$ decay for the inference method for a mandoline with wires one mesh apart placed two mesh lengths from the grid. □ and ×, $\overline{\theta_1^2}$ and $\overline{\theta_2^2}$ with alternate mandoline wires operating, giving two mandolines of configuration (2, 2) at the same distance from the grid, with one mandoline displaced one mesh length laterally from the other; ○, $\overline{\theta_T^2}$ for all mandoline wires operating together with the same current in each wire as for the case when alternate wires were heated; ▽, $\overline{\theta_1\theta_2}$ inferred from the variance decay, (14).

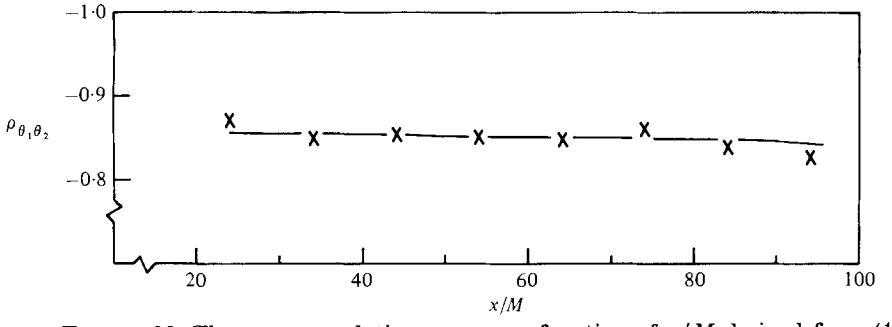

FIGURE 22. The cross-correlation $\rho_{\theta_1\theta_2}$ as a function of x/M derived from (16) for the data of figure 21.

and chimney configurations (2, 2), [2, 2] (figures 2*a*, *b*). For these cases, which are important because they are similar to the way reactants are fed into turbulent flows, the decay of $\rho_{\theta c}$ was slow (figure 17), indicating a slow rate of mixing of the two scalars. In order to simulate this situation by means of the inference method we placed a mandoline two mesh lengths from the grid, with one mesh spacing between the mandoline wires. First the electrical current was passed through every alternate mandoline wire and the variance $\overline{\theta_1^2}$ was measured, then these wires were turned off and the same current was fed into the wires which had previously remained cold and the variance $\overline{\theta_2^2}$ was measured. The situation is as if two mandolines with configuration (2, 2) were

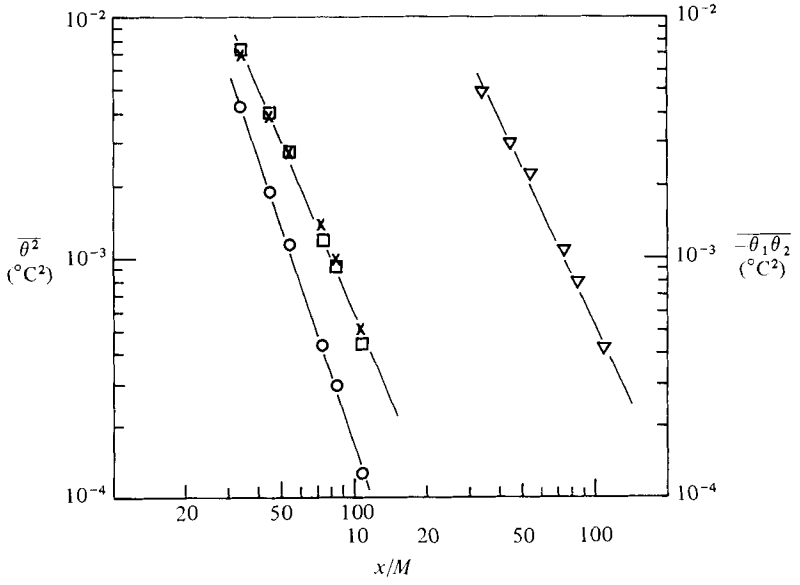

FIGURE 23. $\overline{\theta^2}$ and $\overline{\theta_1\theta_2}$ decay for the inference method for a mandoline with wires one mesh apart placed ten mesh lengths from the grid. □ and ×, $\overline{\theta_1^2}$ and $\overline{\theta_2^2}$ with alternate wires operating giving two mandolines of configuration (10, 2) at the same distance from the grid, with one mandoline displaced one mesh length laterally from the other; ○, $\overline{\theta_T^2}$ for all mandoline wires operating together with the same current in each wire as for the case when alternate wires were heated; ▽, $\overline{\theta_1\theta_2}$ inferred from the variance decay, (14).

positioned such that one mandoline was displaced laterally one mesh length from the other. Note that this is similar to the helium-temperature configuration shown in figure 2(*a*), but with the helium chimneys replaced by another mandoline. Finally both sets of mandoline wires were turned on simultaneously, with the same current in the wires as for the case where the alternate wires were operating. The variance measured for this case is $\overline{(\theta_1+\theta_2)^2} = \overline{\theta_T^2}$. This final situation is as if the mandoline configuration was now (2, 1). The results of the variance decay are plotted in figure 21. $\overline{\theta_1^2}$ and $\overline{\theta_2^2}$ are the same, as they should be, since both are for the same mandoline configuration (2, 2), and with the same current. When both mandolines are operating, however, the variance, $\overline{\theta_T^2}$ is drastically reduced, but the decay rate is approximately the same.† Also shown on figure 21 is the scalar-covariance decay $\overline{\theta_1\theta_2}$ determined from (14). Its decay rate is approximately the same as that of the individual variances.

Figure 22 shows the cross-correlation coefficient inferred from the results of figure 21, i.e.

$$\rho_{\theta_1\theta_2} = [\overline{\theta_T^2} - (\overline{\theta_1^2}+\overline{\theta_2^2})]/[2(\overline{\theta_1^2}\,\overline{\theta_2^2})^{\frac{1}{2}}]. \tag{16}$$

The value of $\rho_{\theta_1\theta_2}$ is approximately $-0{\cdot}85$, and its rate of change is very slow (if at all). Both the negative value and the slow rate of change are in agreement with the

† A similar reduction in temperature variance has been observed in heated-grid experiments: when all the grid bars were heated a smaller temperature variance was observed than when alternate bars were heated with the same current (Warhaft & Lumley 1978*a*, Sreenivasan *et al.* 1980). For an explanation of why the decay rates are approximately the same for the experiments (2, 1) and (2, 2) see the footnote on p. 487. In fact, the decay rate for (2, 1) is slightly slower than for (2, 2) (figure 21). The same anomalous effect was observed when the helium was injected very close to the grid at [2, 1] and [2, 2] (§3.1.2).

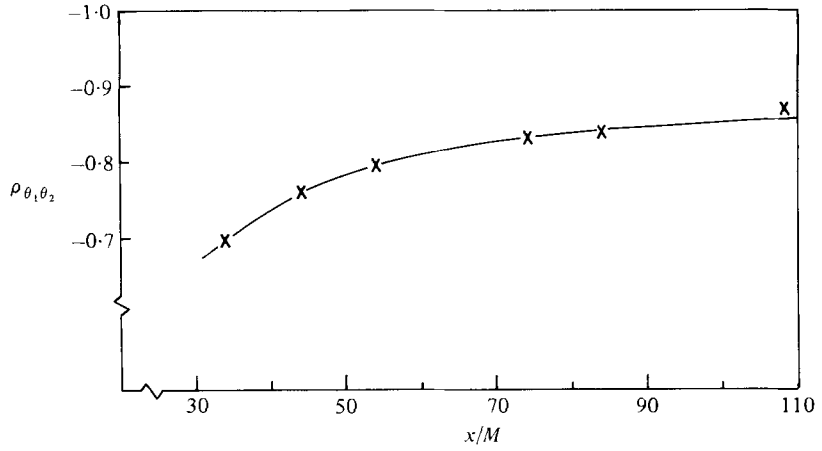

FIGURE 24. The cross-correlation $\rho_{\theta_1\theta_2}$ as a function of x/M derived from (16) for the data of figure 23.

direct method, i.e. with the mandoline and chimney at (2, 2), [2, 2] (figures 2*a* and 17). The large magnitude, however, implies almost-perfect anticorrelation between θ_1 and θ_2. We note that for $\rho_{\theta_1\theta_2} = -1$ the thermal fluctuations would completely disappear (with, of course, the same variance existing when the alternate wires were heated), and thus θ_1 would be exactly equal to $-\theta_2$.

Finally, the above experiment was repeated, but now for the same mandoline (with wires spaced one mesh apart) moved to ten mesh lengths from the grid. Figure 23 shows the variance decays: for the two situations in which alternate wires were heated, $\overline{\theta_1^2}$ and $\overline{\theta_2^2}$ were measured and the decay exponent in (2) was 2·33. When all the wires were heated, with the same current in each wire as used for the cases when alternate wires were heated, the decay exponent has increased to 3·0. This is as would be expected, since now the mandoline configuration is (10, 1) and the higher decay rate occurs since wires are closer together (this result is of course the same as in figure 10, although different heating currents were used there). Note, as for the case when the mandoline was two mesh lengths from the grid, that the magnitude of the variance $\overline{\theta_T^2}$ is much less than when only alternate wires were operating. However, for the case when the mandoline was two mesh lengths from the grid, the decay rates for (2, 2) and (2, 1) were approximately the same (figure 21).

Figure 24 is a plot of the scalar cross-correlation, determined using (16), for the data of figure 23. The cross-correlation *increases* with x/M. This remarkable result is in accord with the decay laws: if the decay law for the two cases for the mandoline (10, 2) is

$$\overline{\theta_1^2} = \overline{\theta_2^2} = A(x/M)^{-m_1}, \tag{17}$$

and that for all wires operating, (10, 1), is

$$\overline{\theta_T^2} = B(x/M)^{-m_2}, \tag{18}$$

then substituting (17) and (18) into (16) we find

$$\rho_{\theta_1\theta_2} = -1(1-(B/2A)(x/M)^{-m_2+m_1}). \tag{19}$$

For the data of figure 23, $\overline{\theta_1^2} \sim \overline{\theta_2^2} = 28{\cdot}2\,(x/M)^{-2{\cdot}33}$ and $\overline{\theta_T^2} = 166{\cdot}4\,(x/M)^{-3{\cdot}0}$, thus

$$\rho_{\theta_1\theta_2} = -1[1-2{\cdot}95\,(x/M)^{-0{\cdot}67}]. \tag{20}$$

Equation (20) shows that $|\rho_{\theta_1\theta_2}|$ will increase and asymptote to a value of -1. Note however that for $m_1 \sim m_2$ (as is for the case depicted in figure 21, mandolines (2, 1) and (2,2)) (19) shows that $\rho_{\theta_1\theta_2}$ will be constant, as is observed (figure 22).

Equation (19) also shows that the form of the $\rho_{\theta_1\theta_2}$ decay depends only on the rate of decay of the individual variances. Since m_2 will always be greater than m_1 (apart, that is, from the special case where the mandoline is placed very close to the grid) because a smaller thermal mesh is associated with a faster variance decay, $|\rho_{\theta_1\theta_2}|$ must always increase for this type of experiment where the scalars are introduced far downstream from the grid in the same plane. The initial magnitude of $\rho_{\theta_1\theta_2}$, however, depends on the ratio $B/2A$, (19), and this ratio could conceivably be changed by changing the relative phases of θ_1 and θ_2, i.e. by changing the spacing between the wires. In the experiments described here the wires were one mesh apart, i.e. approximately a velocity integral scale, and $|\rho_{\theta_1\theta_2}|$ was high. Possibly, if the wires were placed further apart, a lower initial $|\rho_{\theta_1\theta_2}|$ would result, although, as shown above, its magnitude would still increase and asymptote to unity. Further experiments, both wind-tunnel as well as numerical, could shed further light on this aspect.

In summary, if two scalars are fed into the flow at precisely the same scale, and at the same distance from the grid (thus at a position where the velocity length scale is the same for both scalars) the cross-correlation between the scalars will either remain constant, or actually increase, with x/M depending on whether the scalars are introduced close to the grid (figure 22) or further downstream (figure 24). Of course, for both cases the scalar covariance $\overline{\theta_1\theta_2}$ is decreasing, i.e. the covariance is dissipated ((15) and figures 21 and 23). The unexpected case in which the scalar cross-correlation function increases has only been determined using the inference method; it will be interesting to see (in future measurements) whether this result can be verified using two different scalars.

4. Conclusions

Our results show that the evolution of scalar fields in grid turbulence is critically dependent on the way the scalars are fed into the flow. The evolution of the scalar depends on the initial wavenumber (or scale) of the scalar field relative to the initial wavenumber (or scale) of the velocity field. For the case of a single scalar there are only two relevant wavenumbers, those of the scalar and the velocity fields. For the case of two scalars there are three relevant wavenumbers, those of each scalar and the velocity, all of which may be varied independently. Thus the mixing of two scalars is more complex than the mixing of a single scalar. We have found no evidence, however, to suggest that the evolution of the scalar field depends on the initial magnitude of the scalar variance or on the initial magnitude or sign of the cross-correlation coefficient for the cases investigated, which were for passive scalars. Our results, which will be summarized below, have been obtained by two independent methods: for a single scalar both temperature and helium have been used, for two scalars a direct method using c and θ has been compared with an inference method using θ only. The results using the different methods (and scalars) are in good agreement with each other.

The results may be summarized as follows.

(i) As was previously determined (Warhaft & Lumley 1978*a*) for temperature variance, the decay of helium variance depends on the relative scale of the helium

fluctuations to the velocity fluctuations; as the scale of the helium fluctuations is reduced relative to that of the velocity, the decay rate of $\overline{c^2}$ will be increased (figures 12–14). It should be noted that for $r_\theta = r_c = 1$ the scalar length scale, be it for temperature or helium, is greater than the velocity length scale (figure 14). Furthermore, for $r_\theta = r_c$, the helium length scale is greater than the thermal length scale (figure 14). This is thought to be due to the difference in diffusivities of the two scalars.

(ii) The decay of the scalar-flux cross-correlation coefficient, $\rho_{u\theta}$ and ρ_{uc}, is very slow if the scalars are introduced close to the grid, where the scalar length scale is determined by the large-scale mixing of the velocity wakes behind the grid bars, but more rapid if the scalar flux is introduced further downstream. Here the scalar is introduced into approximately isotropic turbulence, and its scale is set independently of that of the velocity (figures 15 and 16).

(iii) The decay of the two-scalar cross-correlation coefficient ($\rho_{\theta c}$ or $\rho_{\theta_1\theta_2}$) is also slow if both scalars are introduced close to the grid, where the scalar length scales are completely determined by the velocity field (figures 17 and 22). If the two scalars are introduced at different longitudinal positions from the grid the decay of the scalar cross-correlation coefficient is much more rapid (figures 17 and 20, and Warhaft 1981). In this case the mismatch between the two scalar scales as well as the difference in velocity scale at the positions where the two scalars are introduced appears to facilitate the more rapid cross-correlation decay rate. Finally, we have presented a case in which the scalar cross-correlation coefficient increases with distance from the grid (figure 24). For this case both scalars were fed into the flow at exactly the same scale (which was smaller than that of the velocity scale) and at the same distance downstream from the grid. Of course, for this case (which was determined using the inference method) the scalar covariance decayed (as it did for all the other cases), i.e. the system was still dissipative, although the increase in $\rho_{\theta_1\theta_2}$ suggests that the scalar fields were becoming more ordered.

Thus the scalar cross-correlation coefficient may decrease, remain constant, or increase with downstream distance, depending on how the two scalars are fed into the flow. This is a remarkable variation for a decaying flow without any production mechanisms and shows how strong the initial conditions are in determining the evolution of the flow in grid turbulence.

We thank Professors J. L. Lumley and S. Pope for discussions, and Mr E. P. Jordan for technical assistance. This work was funded by grants from the Engineering section and the Atmospheric Science section of the U.S. National Science Foundation. The respective grant numbers are MEA-8104733 and ATM 79-22006.

REFERENCES

Antonopoulos-Domis, M. 1981 Large-eddy simulation of a passive scalar in isotropic turbulence. *J. Fluid Mech.* **104**, 55–79.

Comte-Bellot, G. & Corrsin, S. 1966 The use of a contraction to improve the isotropy of grid-generated turbulence. *J. Fluid Mech.* **25**, 657–682.

Durbin, P. A. 1981 Analysis of the decay of temperature fluctuations in isotropic turbulence. Submitted to *Physics of Fluids.*

Gad-El-Hak, M. & Corrsin, S. 1974 Measurements of nearly isotropic turbulence behind a uniform jet grid. *J. Fluid Mech.* **62**, 115–143.

GIBSON, C. H. & SCHWARTZ, W. H. 1963 The universal equilibrium spectra of turbulent velocity and scalar fields. *J. Fluid Mech.* **16**, 365–384.

KERR, R. M. 1981 Ph.D. thesis, Laboratory of Atomic and Solid State Physics, Cornell University.

LARUE, J. C. & LIBBY, P. A. 1977 Measurements in the turbulent boundary layer with slot injection of helium. *Phys. Fluids* **20**, 192–202.

LIBBY, P. A. 1977 Studies in variable-density and reacting turbulent shear flows. In *Studies in Convection*, vol. 2 (ed. B. E. Launder). Academic.

LUMLEY, J. L. 1978 Computational modeling of turbulent flows. *Adv. Appl. Mech.* **18**, 123–176.

NELKIN, M. & KERR, R. M. 1981 The decay of scalar variance in terms of a modified Richardson law for pair dispersion. *Phys. Fluids.* **24**, 1754–1756.

NEWMAN, G. R., LAUNDER, B. E. & LUMLEY, J. L. 1981 Modelling the behaviour of homogeneous scalar turbulence. *J. Fluid Mech.* **111**, 217–232.

NEWMAN, G. R. & HERRING, J. R. 1979 A test field model study of a passive scalar in isotropic turbulence. *J. Fluid. Mech.* **94**, 163–194.

SIRIVAT, A. 1982 Experimental studies of scalar mixing in grid turbulence. Ph.D. thesis, Sibley School of Mechanical and Aerospace Engineering, Cornell University.

SREENIVASAN, K. R., TAVOULARIS, S., HENRY, R. & CORRSIN, S. 1980 Temperature fluctuations and scales in grid-generated turbulence. *J. Fluid Mech.* **100**, 597–621.

STANFORD, R. A. & LIBBY, P. A. 1974 Further applications of hot wire anemometry to turbulence measurements in helium–air mixtures. *Phys. Fluids* **17**, 1353–1361.

WAY, J. & LIBBY, P. A. 1970 Hot-wire probes for measuring velocity and concentration in helium–air mixtures. *A.I.A.A. J.* **8**, 976–978.

WAY, J. & LIBBY, P. A. 1971 Application of hot-wire anemometry and digital techniques to measurements in a turbulent helium jet. *A.I.A.A. J.* **9**, 1567–1573.

WARHAFT, Z. 1980 An experimental study of the effect of uniform strain on thermal fluctuations in grid-generated turbulence. *J. Fluid Mech.* **99**, 545–573.

WARHAFT, Z. 1981 The use of dual heat injection to infer scalar covariance decay in grid turbulence. *J. Fluid Mech.* **104**, 93–109.

WARHAFT, Z. & LUMLEY, J. L. 1978*a* An experimental study of the decay of temperature fluctuations in grid-generated turbulence. *J. Fluid Mech.* **88**, 659–684.

WARHAFT, Z. & LUMLEY, J. L. 1978*b* The decay of temperature fluctuations and heat flux in grid-generated turbulence. In *Structure and Mechanisms of Turbulence II* (ed. H. Fiedler). Lectures Notes in Physics, vol. 76, pp. 113–123. Springer.